IEEE Access
Multidisciplinary | Rapid Review | Open Access Journal

Received June 24, 2020, accepted July 5, 2020, date of publication July 13, 2020, date of current version July 23, 2020.

Digital Object Identifier 10.1109/ACCESS.2020.3008748

Compact, Portable, High-Density Functional Near-Infrared Spectroscopy System for Brain Imaging

M. ATIF YAQUB, SEONG-WOO WOO, AND KEUM-SHIK HONG, (Fellow, IEEE)
School of Mechanical Engineering, Pusan National University, Busan 46241, South Korea

Corresponding author: Keum-Shik Hong (kshong@pusan.ac.kr)

This work was supported in part by the National Research Foundation (NRF) of Korea under the auspices of the Ministry of Science and ICT, South Korea, under Grant NRF-2017R1A2A1A17069430.

ABSTRACT Advancements in functional near-infrared spectroscopy (fNIRS) neuroimaging have extended its usage from clinical settings to real-life applications. We developed a wearable and wireless fNIRS-based neuroimaging system that can be applied for brain disease diagnostics and during daily life activities. We utilized 128 compact dual-wavelength LEDs of 735 nm and 850 nm and a silicon photodiode (SiPD). The LEDs and SiPD were closely assembled in a 3D-printed flexible configuration holder fitted in a soft neoprene cap. The developed configuration has 128 channels in a 7 $\times$ 7 cm area with source-detector separations ranging from 5 mm to 38 mm, which intends to provide a high-density device. The system acquires data from multiple brain depths to generate a 3D activation image. Short-separation channels provide the physiological noise in the superficial layer, which can be used to enhance fNIRS signals. The experimental data are stored in a USB flash disk attached to the device. We developed software that is connected to the device using Wi-Fi to display the oxyhemoglobin (HbO) and deoxyhemoglobin (HbR) levels in real-time. The system architecture allows the selection of channels and the use of multiple devices simultaneously. The system was tested using a silicone phantom as well as human subjects. The LED intensity is dynamically calibrated within the safety range once the device is set up, so that every channel can acquire stable data. The system provided high-quality signals with a signal-to-noise ratio of more than 64 dB, high optical sensitivity, and dynamic optical range of 140 dB in the phantom test. A sampling rate of 30 Hz was achieved with all the channels used. The system exhibited valid HbO and HbR responses during the arterial occlusion test and a motor task. These results show that the developed system can provide precise, robust, and multi-depth measurements resulting in high-density images. With these novel characteristics, the system favors clinical usage and outdoor activities as well as brain-computer interface applications.

INDEX TERMS Multi-depth fNIRS, brain-computer interface, 3D fNIRS, wearable, wireless, real-time display.

I. INTRODUCTION

Developments in the field of neuroimaging technologies are vital to enhance our understanding of human brain operation. Comprehensive interpretation is crucial in finding discrepancies leading to several brain diseases. The healthcare industry is increasingly burdened by degenerating brain diseases. The rise in these brain diseases stems from the aging population. The aging society is significant in developed countries at present, while the developing world will encounter this dilemma soon [1]. To cope with this situation, a noninvasive neuroimaging technology that can provide continuous monitoring is required. Brain imaging can help distinguish different neuronal conditions in various dementias (e.g., Alzheimer's disease, vascular dementia, Lowy body dementia, frontotemporal dementia, Parkinson's disease, etc.), psychiatric disorders, or neurological impairments. Functional magnetic resonance imaging (fMRI) has been a well-established clinical choice for a neuroimaging modality for several decades for diagnosing various diseases.

The associate editor coordinating the review of this manuscript and approving it for publication was Gang Wang.

fMRI has undeniably advanced the understanding of the functional framework of the human brain [2]. fMRI has the advantage of a high spatial resolution with a voxel size of 1–2 mm^3. However, it is plagued with several disadvantages such as poor temporal resolution, non-portability due to bulky size, unaffordability for imaging in natural positions (like moving, sitting, or standing), financial burden, and incompatibility with infants and patients with implants [3]. Therefore, we developed a brain-imaging system that can produce results with high temporal as well as densely configured channels. The presented system is suitable for patients/subjects of all ages in all environments. The proposed system will reduce the financial burden due to continuous monitoring.

Functional near-infrared spectroscopy (fNIRS) is a noninvasive brain-imaging technique that can overcome the drawbacks of fMRI. It is a light-based method, which can efficiently reveal and quantify the activity in the human brain [4]–[7]. A near-infrared source attached to the scalp shoots light, which travels through the superficial layers of head and brain tissues. The photodetectors receive diffused reflective light, and the portion of light detected at the photodiodes is assumed to have traveled through a banana-shaped path from the emitter. The penetration depth of NIR light in the brain tissue depends on the separation between the source and detector [8], [9]. A larger source-detector separation can provide an image of the signal from a deeper brain region, assuming that the detected photons have traveled the deeper region. The attenuation of received light is significantly increased as the distance traveled by the photon increases, which limits the maximum source-detector separation. The changes in received light intensity from a constant NIR source correspond to the concentration changes in oxyhemoglobin (HbO) and deoxyhemoglobin (HbR) [10], [11]. These blood chromophores are the main absorbers in the NIR spectrum and are calculated using the modified Beer-Lambert law (MBLL) [12], [13]. Variations in the HbO and HbR concentrations occur due to the neurovascular coupling mechanism in which neurons draw energy through the network of tiny blood vessels laid out in the brain. Neuronal firing is directly related to regional brain activation, which is commonly perceived by changes in HbO only because it has higher sensitivity over HbR [14]–[16]. However, several studies show that the information provided by HbR cannot be altogether neglected, and the combined information is important in computing local brain activity [17]–[20]. Furthermore, the quantitative information can be used to assess the cerebral blood volume and the tissue oxygenation index, which strengthens the revelation of hemodynamic activation [21].

The detection of small light intensities is a challenging task that requires highly sensitive equipment. Avalanche photodiodes or photomultiplier tubes are recommended because of the high photosensitivity, and they are a popular choice for expensive and stationary fNIRS machines that operate at high voltages [22], [23]. However, those machines are unsuitable for compact wearable devices. Silicon photodiodes are commonly utilized in wearable devices because they are available in small sizes and can be operated at low voltages. They are extremely economical when compared to the avalanche photodiodes or photomultiplier tubes. Wearable and cost-effective fNIRS devices can be applied at home by patients with various brain disorders. They can be used to monitor the neuronal health of patients with impaired brains daily while performing different tasks in unrestricted environments [24]–[26]. This will reduce the current healthcare burden for the rising number of brain diseases with innovative solutions where telemedicine and self-examination will be possible. The wearable technology can also be utilized as a brain-computer interface (BCI) [27]. BCIs are involved in maneuvering assistive or rehabilitative robots or communication by brain-impaired patients. EEG is another popular option for BCI, but fNIRS with better spatial resolution and robustness to electronic noise can prove to be more fruitful [28]–[31].

The fNIRS signal is prone to multiple physiological noises. As light travels through superficial layers, it induces changes from these layers which do not relate to functional information. Short-separation channels are one of the highly effective methods to remove systemic physiological noise [32]–[34]. These short-separation channels have a source-detector separation of less than 1 cm [35]. Therefore, only physiological effects are captured by these channels. The information from these channels can be subtracted from conventional long-separation fNIRS channels to acquire a clean signal [36], [37]. Although the integration of short-separation channels in the conventional channel configuration requires extra components, it can significantly improve the signal quality by removing physiological noises. In addition, most fNIRS equipment can only be used to monitor brain areas with a reasonable spatial resolution that is lower than fMRI. For high-resolution imaging using fNIRS, many channels should be configured in a closely-knit fashion, and the optodes should be placed very close to each other [38], [39]. This creates a large dataset for fNIRS, unlike the dataset created by conventional limited channels. The created dataset can be processed by complex algorithms like neural networks, which require large datasets [40]–[43]. This type of configuration utilizes multiple source-detector separations, which results in light penetrating multiple depths in the brain. The depth information can be incorporated in the output to deliver a 3D functional brain image.

In this study, we describe the design and development of a densely-configured fNIRS system that extends the current continuous-wave fNIRS framework. The device is economical, battery-operated, portable, and wearable. It can be operated wirelessly to ensure use in open environments beyond any restrictions. The system incorporates short-separation channels along with long-separation channels to provide a wide range of source-detector separation of 5 mm to above 38 mm. This is the first wearable system to incorporate a large number of sources and detector to create densely positioned channels targeting various depths in the brain to generate a

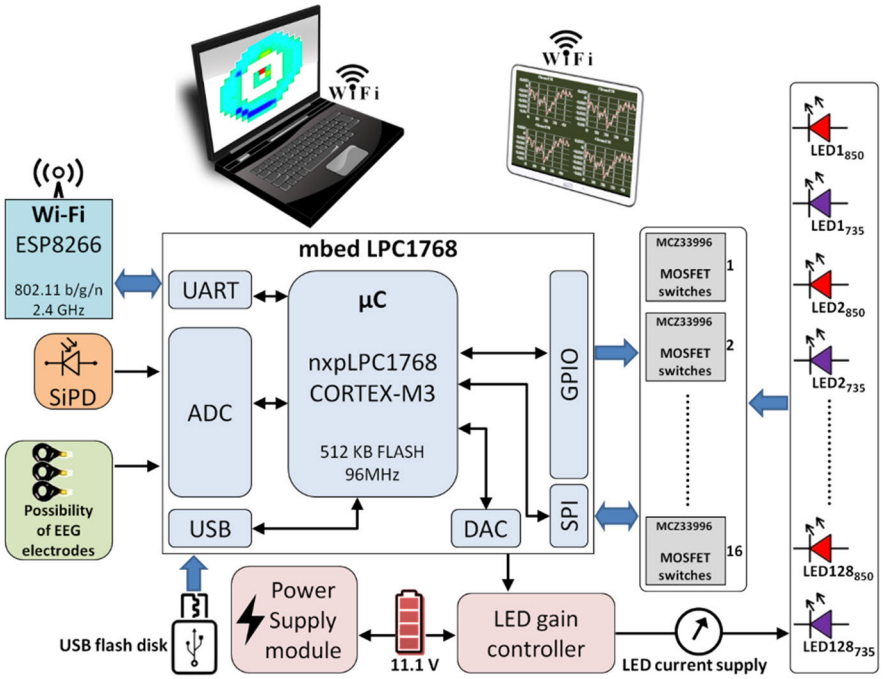

FIGURE 1. Simplified block diagram showing components and modules used in the system.

3D brain activation image with high temporal resolution. The system is extendable for multimodal fNIRS-EEG imaging. The system provides a graphical user interface (GUI)-based software, which computes and displays blood chromophore levels in real-time. Multiple brain regions can be studied simultaneously using multiple devices. The developed system with a unique combination of these features will extend the application of fNIRS technology as an open-environment friendly option. In the following sections, the principle and technical details of the system are provided in detail. We also report the preliminary validation of the system's performance through phantom and human-subject-based measurements.

II. METHODOLOGY

To observe the neuronal activation using the fNIRS-based system in a free environment, the system should have a reduced form factor and wireless communication. This will allow portability, wearability, configurability, and battery-operated power supply. The system requirements exponentially increase when the source-detector combinations increase. This includes real-time data processing and storage, information transmission, and visualization of measured chromophores. These qualities make the system design a challenging task. A high signal-to-noise ratio (SNR) is required for such systems to accurately measure the changes occurring in the brain. A higher sampling frequency is crucial in constructing a reliable signal by rejecting the influence of various noises. Continuous brain monitoring for longer durations also emphasizes the safety aspect of the system. The system must involve user-protection at all levels so that it does not harm the patient electrically (current), thermally (heat), optically (intensity), or mechanically (headgear and device enclosure). The system should be user-friendly with an easy-to-understand GUI for smooth and convenient operation and a comfortable headgear embodying the sources and detectors. Various experimental paradigms require different area coverage of the brain; therefore, the system should be modular and configurable such that multiple devices with selective channels can be used simultaneously.

A. SYSTEM ARCHITECTURE

The system overview is pictorially presented in Fig. 1. The system is a combination of our developed software and hardware modules. A Windows-based computer hosts the software, which communicates wirelessly with the embedded system. The electronics of our designed embedded system reside on a single board. The headgear containing NIR light sources and a photosensor is attached to the board. The board houses various modules that include light switching and gain adjustment, photosensor interfacing, wireless communication, USB storage, power supply, and, most importantly, command and control. The details of these modules are provided in subsequent subsections. Serial peripheral interface (SPI) and universal asynchronous receiver transmitter (UART) protocols are used in the embedded system for communication between devices.

B. NIR LIGHT SOURCE MODULE

NIR light sources are one of the most critical parts of an fNIRS device. They are the interface between the scalp and the machine. The imaging result considerably depends on the type of the source, its attachment with the skin, and the

stability of the current supplied to the source. The curved shape of the human head and hair are significant challenges in coupling the sources to the scalp. If the sources are not properly placed, the light entering the head can leak toward the photosensor, producing unreliable results. These key aspects of usability should also be monitored so that the subject under study feels comfortable. The incoherent and uncollimated light output makes the LED a safer choice. In addition, the laser diodes require additional temperature measurements and control, which is not suitable for a portable system. We utilized dual-wavelength LEDs (SMT735D/850D) with a narrow spectrum ($\Delta\lambda < 30$ nm) for both wavelengths provided by Marubeni America Corporation, USA. The wavelengths (735 nm and 850 nm) were selected based on previous studies to prevent signal contamination due to crosstalk [44], [45]. These wavelengths are adequate in computing the desired chromophores, that is, HbO and HbR. This precise LED was also selected because of the incentive of a small package.

In the designed fNIRS system, we used 128 dual-wavelength LEDs, i.e., 256 NIR light sources. To control the switching of this large number of NIR sources, SPI-based low side switching IC (MCZ33996) was applied. An LED source of dual wavelengths has a compact size of 2.7 $\times$ 3.5 mm. This IC is operated with a 3.3 V logic level, which allows the flow of sharp currents. Each IC has 16 available outputs, and 16 ICs are employed to control the switching of the 256 NIR sources arranged in the headgear. The cathodes of all LEDs are connected to the output pins of the switching IC. Once the IC is configured, a 24-bit command is received to allow current to flow through a specific LED. The LEDs are switched on using time multiplexing technique, where only a single source is powered at a time. The LEDs follow the round-robin sequence for switching.

The LED intensity depends on the supplied current. Light absorption differs according to various skin colors [22]. In addition, the brain location under observation is an important factor for the required light intensity. The light intensity should be such that it can cross the scalp and skull to reach the brain [46]. Therefore, gain adjustment for the NIR source is required to develop a device that can be used to study all the brain areas. A single stabilized current driver, which is a combination of op-amp and transistor, is utilized to supply current to all the 256 NIR sources. The current driver adjusts the current for each wavelength of every LED individually. The gain of the current driver is controlled by a digital-to-analog converter (DAC). The DAC output is supplied to the current driver, thus varying the intensity of light sources within the safety limits. The safety limit must be strictly adhered to because going beyond the safety limit can cause redness of skin, skin irritation, or skin burn in severe cases. Stable light intensity is also critical to detect the changes in chromophores. A variation in source intensity cannot be distinguished from the changes occurring because of absorption by blood chromophores. Therefore, the NIR source driver should be compulsorily robust.

C. PHOTOSENSOR MODULE

The photosensor, other than the NIR light source, is the most important component of the fNIRS system because it is also the interface between the skin and the machine. We utilized a single silicon photodiode (SiPD) to design the photosensing system because it is appropriate for our objectives of portability and economic efficiency. It is suitable for rapid data acquisition for a faster fNIRS imaging frame rate. The selected SiPD (S12158-01CT) was provided by Hamamatsu Photonics, Japan. The SiPD package has a compact size of 4.2 $\times$ 4.2 mm. It has a substantial photosensitive area of 2.77 $\times$ 2.77 mm, which is appropriate to detect the reflected NIR light from the brain cortex. The selected chip-on-board type package has a good ratio of package size to the photosensitive area. The utilized SiPD has a high sensitivity for both the NIR source wavelengths utilized in our design. A high SNR is mandatory in fNIRS-based brain imaging. Several factors affect the quality of signals obtained during the actual human subject-based experiments, which include source-detector separation, light intensity, physiological noises, ambient noise, sampling frequency, skull thickness, and skin tone. Therefore, special care should be taken in designing and placing the SiPD interface circuit.

Signal digitization is required for designing an fNIRS system. An analog signal is generated as the reflected light reaches the surface of a SiPD. Upon the arrival of NIR light, a tiny current is generated, which is amplified considerably before reaching the analog-to-digital converter (ADC) terminal. A shielded cable is carefully used in the design to secure the acquired signal from being contaminated by environmental noises as it travels from the headgear to the designed device board. We employed an onboard 12-bit successive approximation type ADC. To achieve a high sampling rate with a large number of NIR sources, the SiPD was used in photoconductive mode. A filter circuit was used to block the effects of high-frequency noise from the voltage supply. The amplifier gain was static for SiPD, whereas the NIR source gain was dynamic. Therefore, the SiPD interface circuit can provide substantial value for each of the 256 NIR sources.

D. WIRELESS COMMUNICATION MODULE

If a device can transfer data wirelessly to a monitoring console, it can be used freely in any environment. We used an ESP8266 Wi-Fi module for incorporating portability in our system. The Wi-Fi module was only employed in the case of real-time monitoring of neuronal activation. The module receives fNIRS data using a universal asynchronous receiver-transmitter (UART) that is transferred to the monitoring console, which is a personal computer in our design. It is a low power board requiring 3.3 V operating voltage. This module is small and compact because of the onboard printed antenna for transmission and receiving signals. The small footprint allows painless integration in our device.

E. USB STORAGE MODULE

An onboard USB interface is used to connect the USB flash disk for data recording purposes. Data recording is mandatory for offline data processing. In fNIRS-based neuroimaging studies, data are recorded, which are analyzed later. The USB storage allows small disk drives to be attached to the designed embedded system for data recording. Additionally, data extraction from the device to a computer for processing does not require the device to be accessed. The USB flash disk has data files that can be copied easily. The intensities of the NIR source light received by the SiPD are stored in text files that can be readily transferred to processing software or used to compute HbO and HbR levels.

F. POWER SUPPLY MODULE

The power supply module provides multiple voltage levels required by all devices and circuits throughout the designed board. The module supplies 9, 5, and 3.3 V to the switching ICs, Wi-Fi module, controller board, USB storage, LED driver, and SiPD amplification. The system controls the shooting of 256 NIR light sources, which requires a stable and rugged power source. A compact 11.1 V lithium-ion battery is used to meet the power requirements of the system. The battery has a capacity of 1500 mAh, which allows long duration experiments. The use of a battery is imperative for wearable mobile devices. The option of an alternate power source through a 9 V adapter is also integrated into the system, and a dedicated jack is attached to the designed board. This source is useful during device testing or when the system is not used in a mobile configuration.

G. COMMAND AND CONTROL MODULE

Every embedded system must have a dedicated module for controlling the flow of the system. We used a powerful rapid prototyping board, mbed LPC1768, provided by Arm Limited, United Kingdom, in our designed system. This module communicates with all the aforementioned modules. It is a compact board that has a 40-pin DIP package, which allows easy attachment on the board. The module has various interfaces, among which we utilized digital output, SPI, UART, ADC, DAC, and USB. The mbed LPC1768 board is powered with 9 V from the power supply module. It is responsible for shooting and controlling the intensities of LEDs, receiving data from SiPD, storing data in the USB flash disk, and transferring the data to the monitoring console. A state machine is designed and implemented in the onboard microcontroller, LPC1768, provided by NXP Semiconductors N.V., Netherlands, to control the flow of the system, as shown in Fig. 2.

The microcontroller (master) communicates with 16 switching ICs (slave) using SPI. An independent slave control architecture is employed where the microcontroller addresses each switching IC individually. Sixteen digital outputs from the controller board are used for individual selection of switching ICs using their corresponding chip-select pins. The microcontroller configures the SPI for

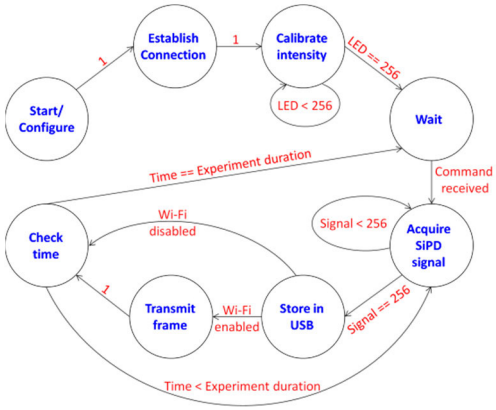

FIGURE 2. State machine for fNIRS device.

switching ICs and sends a 24-bit command for switching each NIR source. The calibration of low-signal channels can be done at each experiment by adjusting the LED intensities automatically. The intensity for every LED is adjusted in the configuration state using DAC to generate a ramp-up signal until the SiPD signal value reaches the desirable range. Thus, the supply source of LEDs becomes a ramp-up current source. The final gains for individual LEDs are stored for use during the experiment. The gain can only be increased within the safety range, which ensures that the sources do not become hot even after long experiment duration. In case the light from any NIR source measured by SiPD does not reach the desired stable range, both wavelengths from that source are marked to be discarded, and a channel is lost. This information allows the user to start with a few channels or restart the experimental protocol after checking the headgear.

The microcontroller board can digitize five analog inputs. A single ADC channel is utilized in our design. The 12-bit ADC has a resolution of detecting a minimum change of 805 μV. The sampling rate of ADC is critical in defining the frame rate of our system. A full-frame is the combination of intensities of received light from all 256 LEDs. A maximum of 40 Hz can be achieved with the full-frame. This means that the acquisition from 256 sources can be completed in less than 25 ms. The system can integrate four EEG electrodes for hybrid fNIRS-EEG imaging by utilizing four vacant onboard ADC pins. This allows the system to measure the electric potential from active EEG electrodes. This compatibility allows the design of a wearable multimodal fNIRS-EEG system.

When a single frame measurement is completed, the 256 digital light intensities are stored in a USB flash disk. During the configuration state, a text file is made in the USB flash disk that we keep appending with new data after every frame acquisition. The file is closed when the experiment is completed. The complete frames are also transferred to the computer using the Wi-Fi module. The Wi-Fi connection is established between the designed embedded system and the computer during the configuration state. The microcontroller continuously sends data to the Wi-Fi module using UART

after every frame acquisition. Each measured light intensity is 16-bit wide and stored in a 16-bit memory. The UART of the Wi-Fi module receives the 8-bit data; therefore, the intensity is broken into two separate bytes. The two bytes that represent a single value are transferred successively.

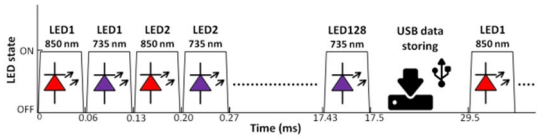

FIGURE 3. Visual representation of LEDs' sequence and timing for data acquisition and recording.

All sources are powered down during the configuration state. The SiPD reads the NIR light in the order of 850 nm and 735 nm from the first LED package, then from the second LED package, and continues until the last LED package. Then, it restarts from the first, as shown in Fig. 3. It takes 0.13 ms to shoot both wavelengths from an LED package and their measurement through SiPD. For measuring a complete frame, 17.5 ms are required, while its storage in the USB disk takes 12.0 ms. The system can acquire data at a stable rate of 30 Hz for the full-frame. For a reduced number of channels, the sampling rate can be even higher and can go up to 3.2 kHz for a single channel.

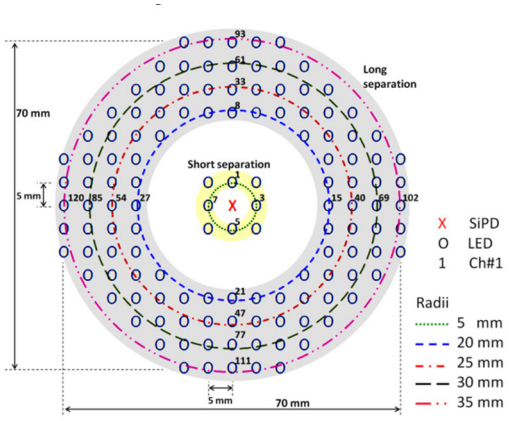

FIGURE 4. Channel configuration of the device: The channel number increases in the clockwise direction.

H. OPTODE CONFIGURATION AND 3D IMAGING

We designed a novel high-definition configuration, as shown in Fig. 4. A total of 128 LED packages were arranged around a single SiPD located in the center, covering an area of 7×7 cm, using the bundled-optode method of configuration design [38]. The separation between two successive LED packages is 5 mm. This configuration significantly improves the spatial density, which allows the measurement of neuronal activation with more data points within a focused region. An fNIRS channel is formed between the SiPD and each LED source. Therefore, a total of 128 channels are formed in the designed configuration. Among the 128 channels, eight channels are short-separation channels, where the distance between the SiPD and an LED source is less than 10 mm. The integration of these channels is advantageous as they are utilized to remove physiological effects from the channels carrying information regarding brain activation. Short-separation channels capture the physiological effects from the superficial layers (scalp, skull, cerebral spinal fluid) and not from the brain. These effects can be subtracted from the long-separated channels that capture the effects from the brain as well as the superficial layers [37]. The subtraction can be performed after applying a scaling factor to the short-separation channel. The scaling factors for each channel can be computed by measuring the correlation between the long and short channels [26]. The LEDs are arranged at variable distances from the SiPD starting from 20 mm, which results in channels reaching different depths in the brain compared to the channels reaching the same depth in the conventional fNIRS imaging; this allows 3D brain imaging using fNIRS. To realize a 3D image, the measured point by each channel is assumed to be the midpoint between the source and the detector, and the depth of the measured point is assumed to be half of the distance [47]. Using this approach, the channel information can be displayed in the 3D space. If the SiPD is located at the origin and the LED sources are placed in the xy-plane, each quadrant shows a mirror image of its neighbor. With the negative z-axis going into the brain, the locations of long-separated channels are computed in Table 1. The resultant channel locations in the 3D space are shown in Fig. 5.

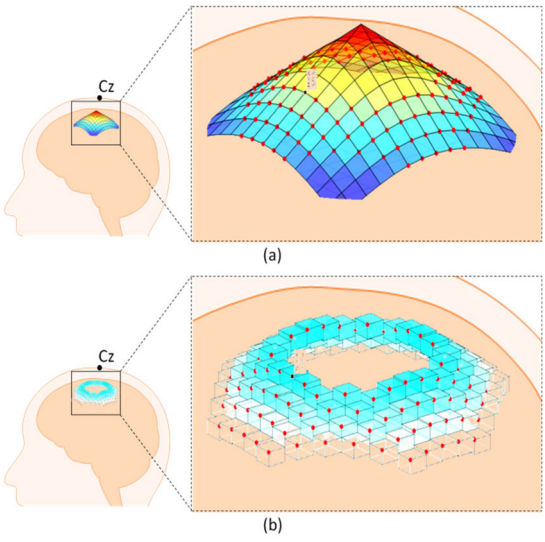

FIGURE 5. Channel configuration in the 3D space mapped on the head: a) The conical surface, and (b) voxel form where the red dots are the center points of the channels represented in (a).

The head surface was assumed locally flat in the brain part covered by the configuration. In this configuration, there are no overlapping channels. To visualize volumetric imaging, a rectangular volume can be used, whose edges are located at locations of the aforementioned channels, as shown in Fig. 5(b). The x- and y-dimensions of the volume are constant throughout the image, whereas small variations occur in the z-dimension. Each rectangular volume represents a single

TABLE 1. Location of long–separation channels.

Ch#	X (cm)	Y (cm)	Z (cm)	Ch#	X (cm)	Y (cm)	Z (cm)	Ch#	X (cm)	Y (cm)	Z (cm)
9	0.00	1.00	–1.00	49	–0.50	–1.25	–1.35	89	–1.00	1.00	–1.41
10	0.25	1.00	–1.03	50	–0.75	–1.00	–1.25	90	–0.75	1.25	–1.46
11	0.50	1.00	–1.12	51	–1.00	–0.75	–1.25	91	–0.50	1.50	–1.58
12	0.75	0.75	–1.06	52	–1.25	–0.50	–1.35	92	–0.25	1.50	–1.52
13	1.00	0.50	–1.12	53	–1.25	–0.25	–1.27	93	0.00	1.75	–1.75
14	1.00	0.25	–1.03	54	–1.25	0.00	–1.25	94	0.25	1.75	–1.77
15	1.00	0.00	–1.00	55	–1.25	0.25	–1.27	95	0.50	1.75	–1.82
16	1.00	–0.25	–1.03	56	–1.25	0.50	–1.35	96	0.75	1.50	–1.68
17	1.00	–0.50	–1.12	57	–1.00	0.75	–1.25	97	1.00	1.25	–1.60
18	0.75	–0.75	–1.06	58	–0.75	1.00	–1.25	98	1.25	1.00	–1.60
19	0.50	–1.00	–1.12	59	–0.50	1.25	–1.35	99	1.50	0.75	–1.68
20	0.25	–1.00	–1.03	60	–0.25	1.25	–1.27	100	1.75	0.50	–1.82
21	0.00	–1.00	–1.00	61	0.00	1.50	–1.50	101	1.75	0.25	–1.77
22	–0.25	–1.00	–1.03	62	0.25	1.50	–1.52	102	1.75	0.00	–1.75
23	–0.50	–1.00	–1.12	63	0.50	1.50	–1.58	103	1.75	–0.25	–1.77
24	–0.75	–0.75	–1.06	64	0.75	1.25	–1.46	104	1.75	–0.50	–1.82
25	–1.00	–0.50	–1.12	65	1.00	1.00	–1.41	105	1.50	–0.75	–1.68
26	–1.00	–0.25	–1.03	66	1.25	0.75	–1.46	106	1.25	–1.00	–1.60
27	–1.00	0.00	–1.00	67	1.50	0.50	–1.58	107	1.00	–1.25	–1.60
28	–1.00	0.25	–1.03	68	1.50	0.25	–1.52	108	0.75	–1.50	–1.68
29	–1.00	0.50	–1.12	69	1.50	0.00	–1.50	109	0.50	–1.75	–1.82
30	–0.75	0.75	–1.06	70	1.50	–0.25	–1.52	110	0.25	–1.75	–1.77
31	–0.50	1.00	–1.12	71	1.50	–0.50	–1.58	111	0.00	–1.75	–1.75
32	–0.25	1.00	–1.03	72	1.25	–0.75	–1.46	112	–0.25	–1.75	–1.77
33	0.00	1.25	–1.25	73	1.00	–1.00	–1.41	113	–0.50	–1.75	–1.82
34	0.25	1.25	–1.27	74	0.75	–1.25	–1.46	114	–0.75	–1.50	–1.68
35	0.50	1.25	–1.35	75	0.50	–1.50	–1.58	115	–1.00	–1.25	–1.60
36	0.75	1.00	–1.25	76	0.25	–1.50	–1.52	116	–1.25	–1.00	–1.60
37	1.00	0.75	–1.25	77	0.00	–1.50	–1.50	117	–1.50	–0.75	–1.68
38	1.25	0.50	–1.35	78	–0.25	–1.50	–1.52	118	–1.75	–0.50	–1.82
39	1.25	0.25	–1.27	79	–0.50	–1.50	–1.58	119	–1.75	–0.25	–1.77
40	1.25	0.00	–1.25	80	–0.75	–1.25	–1.46	120	–1.75	0.00	–1.75
41	1.25	–0.25	–1.27	81	–1.00	–1.00	–1.41	121	–1.75	0.25	–1.77
42	1.25	–0.50	–1.35	82	–1.25	–0.75	–1.46	122	–1.75	0.50	–1.82
43	1.00	–0.75	–1.25	83	–1.50	–0.50	–1.58	123	–1.50	0.75	–1.68
44	0.75	–1.00	–1.25	84	–1.50	–0.25	–1.52	124	–1.25	1.00	–1.60
45	0.50	–1.25	–1.35	85	–1.50	0.00	–1.50	125	–1.00	1.25	–1.60
46	0.25	–1.25	–1.27	86	–1.50	0.25	–1.52	126	–0.75	1.50	–1.68
47	0.00	–1.25	–1.25	87	–1.50	0.50	–1.58	127	–0.50	1.75	–1.82
48	–0.25	–1.25	–1.27	88	–1.25	0.75	–1.46	128	–0.25	1.75	–1.77

voxel similar to fMRI. The x- and y-dimensions of each voxel are 2.5 mm.

I. GUI MODULE

An embedded system used by humans essentially needs a user-friendly and robust operating interface. A Windows-based desktop application was developed using Microsoft Visual Studio, which provided the GUI. This software can receive, compute, display, and record the fNIRS data in real-time. The data, which were stored in the USB flash disk by the wearable device, can be converted to HbO and HbR levels by this GUI.

For Wi-Fi network communication, a transmission control protocol (TCP) is used because of its reliability. A connection is established between the software and hardware after security verification to ensure the legitimate software is connected with our designed embedded system. The GUI sends the current time and date to the wearable device, which is used to name the data file saved in the USB disk. Furthermore, the user can select the type of configuration from a list of predefined channel configurations. The user can set whether he wants the data to be displayed in the software, or he only wants the data to be recorded in the wearable device for the desired duration. In case a data display is required, the software shows the time-series signals of HbO and/or HbR or the activation map of the brain area under study. The time-series signals for a maximum of 16 channels can be shown simultaneously in separate plots. Data visualization is hampered

when more than 16 channels are shown because the graph size becomes very small. The channels to be displayed can be selected from a list of available channels. The activation map is generated based on the relative HbO. The intensity of activation is proportional to the HbO level because neuronal activation is linked with elevated HbO levels [48], [49]. The depth information is also embedded in the image, which is based on the length of the channel, i.e., source-detector separation. It allows channels with a specific depth as well as all channels to be displayed together. Each channel is represented by 25 pixels (5 × 5 px) in the activation map. The smoothing filter is used to generate the activation map such that the edges of each channel are not shown. The Wi-Fi connection is terminated upon completion of the experiment.

The data are transferred to the software frame by frame. The data in the frame received by the software are in the ASCII format, which is a single byte. The frame is processed by consolidating every two successive bytes to give a 16-bit wide integer because each of the original intensity values wes 16-bit wide. The data from both wavelengths are stored in the program memory separately and used for conversion to the HbO and HbR levels in real-time. This converted data are displayed in real-time as well as stored on the computer. Data conversion is performed by implementing the theory of MBLL [50]. The values of differential pathlength factor, based on the wavelengths, were taken as 6.3125 and 5.235 for 735 and 850 nm. The software can compute the absolute concentration of HbO and HbR because of the novel source-detector configuration, in which the absolute values were computed by implementing the bundled-optode theory [38], [47]. The HbO and HbR values for the short-separation channels are not used for real-time noise removal by the software. These values are only stored for offline processing. The measured light intensity file stored by the wearable device and the GUI are formatted identically. The GUI provides the option to convert these files to HbO and HbR.

J. HEADGEAR

Headgear design is very important for any fNIRS system. The headgear must provide the absolute coupling of sources and detectors with the scalp. Ambient light must be blocked because it can distort the effort for acquiring brain activation data. The holding of a large number of optodes in the headgear design is a challenging task [39]. A flexible pad was designed to be manufactured using a 3D-printing facility, as shown in Fig. 6. Multiple design iterations were performed to select the thickness of the pad. A 3 mm thickness was used to provide the best combination of flexibility and durability. The 3D-printed configuration holding pad fits in a square area of 90 × 90 mm. The pad contained hollow boxes of 5 × 5 mm (including a 0.5-mm separation wall), which houses the LEDs and SiPD. Each hollow box had tiny holes that allow the electric wires soldered with the LEDs or SiPD to pass through. The wires connecting the headgear and embedded device were covered with flexible cable holders. The 3D-printed pad was placed inside a neoprene cap, which the human subject can wear. The pad can easily bend inside the cap according to the shape of the head and does not irritate the subject even during a long experiment. The integration of square-shaped EEG electrodes that can fit in the LED package is possible for multimodal imaging.

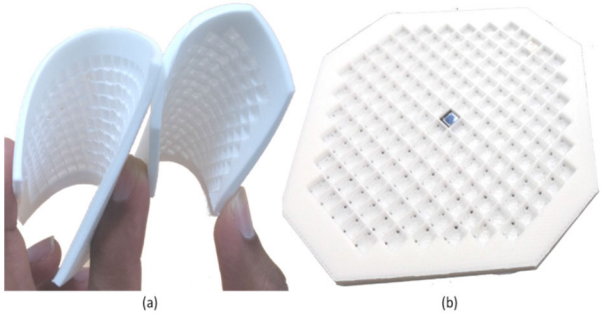

FIGURE 6. (a) The 3D-printed configuration holder is flexible to fit the spherical head, (b) the SiPD is placed in the center, and every box has holes for wires.

TABLE 2. Optical properties of optical silicone phantom used for validation measurements.

Wavelength	μ_a (mm^{-1})		μ_s (mm^{-1})	
	Phantom	Brain	Phantom	Brain
690 nm	0.0104	0.0178	1.15	1.25
830 nm	0.0093	0.0186	1.04	1.11

K. PHANTOM TEST

The developed system was evaluated to verify the reliability in obtaining hemodynamic changes. An optical phantom mimicking the absorption and scattering properties of the human brain was used to evaluate device performance. A silicone phantom provided by ISS Inc., Illinois, USA, with known absorption and scattering characteristics, was employed. Table 2 shows the coefficients of the phantom in comparison with those of the brain (gray and white matter combined) [46]. High-quality data acquisition of raw light intensities is critical to attaining reproducible and reliable HbO and HbR levels. SNR was computed to evaluate the effect of noise in computing the desired chromophores. SNR was calculated as $20 \log_{10}(m/\sigma)$, where m is the mean value and σ is the standard deviation of the measured signals [26]. The measurements from all channels were acquired using the phantom, which was placed inside a box in which ambient light could not enter. The original sampling frequency and configuration were used for these experiments. Many optical devices face the problem of optical drift after long data acquisitions due to temperature changes. Therefore, this drift was computed by measuring the slope for the data of 1 min after the continuous acquisition of 10 min. The normal data acquisition routine for all channels was followed for the slope measuring test. The noise equivalent power (NEP) of the SiPD was used to measure the optical sensitivity. NEP was calculated as I/R, where I is the dark current with no LED light on and R is the responsivity of the SiPD for a given wavelength [51]. The dynamic optical range was evaluated

by increasing the power of LED to the extent where the SiPD did not undergo saturation. The ratio of maximum intensity and NEP, calculated in decibels as $20 \log_{10}(P_{max}/NEP)$, is the dynamic optical range, where P_{max} is the maximum optical power of LEDs [26]. The silicone phantom is a static medium; therefore, light intensity signals were used for measuring the test metrics.

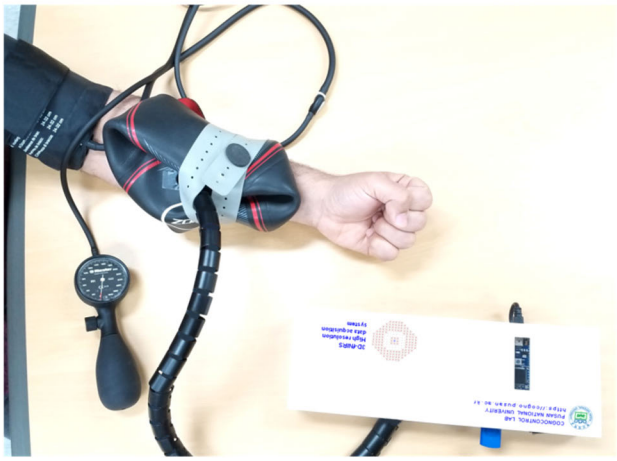

FIGURE 7. Setup for an arterial occlusion test: The cap is tied on the arm, while the gray elastic band ensures coupling of sources and the detector with the skin (the device is placed on a table).

L. ARTERIAL OCCLUSION TEST

The device was tested on a human subject to verify its ability to measure the correct hemodynamic response in situations when the desired output is known. For this purpose, an arm arterial occlusion test was performed. The headgear was adjusted for attachment with the forearm, as shown in Fig. 7. The intensity of light was adjusted in the configuration state such that the SiPD could receive an adequate amount of NIR light. The occlusion caused the HbO to decrease while the HbR increased because the oxygen was consumed constantly while no further oxygen was supplied. Once the supply is allowed, the trend of HbO and HbR will be reversed because HbO will increase while HbR will decrease [24]. Occlusion was observed for 120 s by applying pressure using a manual cuff. The occlusion was repeated three times, and every time, it was followed by a resting state of 180 s. The arm was kept stationary on the table while the subject was comfortably seated in a chair during the whole experiment in a dark room. Four channels were utilized with LEDs that are in a straight line with source-detector separations of 20, 25, 30, and 35 mm. A Velcro band was used to tightly fix the configuration on the arm, and a black fabric was utilized to block ambient light. The measured chromophores were filtered with a low pass filter with a cutoff frequency of 1 Hz.

M. BRAIN ACTIVATION TEST

The capability of our designed system for detecting cerebral hemodynamic changes was evaluated. Neuronal activation was observed on a human subject during a motor execution task. The configuration was placed to cover the left motor cortex. The area of C3 was the desired region of interest. The subject was asked to tap his right-hand fingers at a comfortable pace. A total of 10 trials were performed. Each trial consisted of a task duration of 10 s followed by a resting period of 20 s. The subject was asked to continuously tap his right hand during the task duration and remain calm while looking at the screen. An initial resting period of 60 s was observed before the start of trials. Therefore, the complete experiment lasted for 360 s. The headgear was worn by the subject, and good scalp coupling was observed for all channels. The SiPD values were reported to reach the desired range, indicating proper light reception from all sources. The subject was comfortably seated in a dark room with the instruction screen at a distance of 90 cm. The subject's arm was kept on the table with foam under his hand to reduce vibrations generated by finger tapping. The subject was instructed to stay silent and stationary to avoid contamination by motion artifacts. The data were acquired at a sampling rate of 30 frames per second (FPS). The hemodynamic signals were filtered to remove various kinds of noises using a fourth-order Butterworth low- and high-pass filter with cutoff frequencies of 0.15 and 0.01 Hz, respectively [5]. The channel showing prominent hemodynamic changes was selected as the representative channel.

FIGURE 8. The wearable device can be placed in a backpack while the subject can wear the headgear and move freely.

III. RESULTS

The technical performance of the designed system was evaluated and is summarized in Table 3. The system shows a fruitful combination of SNR, sampling rate, power consumption, wearability, and safety. The wearability of the developed device is shown by a walking person in Fig. 8. The size of the board is $28 \times 7 \times 2$ cm without casing and $29 \times 10 \times 5$ cm including the mechanical casing. The weight of the embedded system, including the casing, is 455 g, and the complete wearable system, including the headgear, is 674 g. The wavelengths were selected to minimize the optical crosstalk for the computation of HbO and HbR [44], [45]. Power consumption is important for a wearable

TABLE 3. Specifications of developed fNIRS system.

Spectroscopic technique	Continuous wave
NIR source	128 LEDs (735 nm, 850 nm)
Detector	1 SiPD (photosensitive area: 2.77 × 2.77 mm)
Number of channels	120 long separation 8 short separation
Source-detector separation	5 mm ~ 36.4 mm
Sampling rate (128 channels)	30 Hz
Maximum sampling rate	3.2 kHz
Device size	Board only: 28 × 7 × 2 cm Encased board: 29 × 10 × 5 cm
Device weight	Encased board: 455 g Complete device with a headgear: 674 g
Headgear	3D printed configuration on flexible neoprene cap
SNR [26]	> 50 dB, including all channels
Noise equivalent power [51]	735 nm: 1.79 nW 850 nm: 1.50 nW
Dynamic optical range [26]	735 nm: 138 dB 850 nm: 140 dB
Optical drift	After 600 s, < 0.001%/sample
Software included	Windows based GUI
Power (128 channels)	< 3.5 W
Battery	Li-ion 11.1 V

system and depends on device usage. The selection of channels, light intensities from NIR sources, received light by SiPD, and real-time display are major factors affecting the required power. The power consumed by the device with complete frame acquisition was less than 3.5 W.

The noise equivalent power (NEP) was determined for both wavelengths and was found to be 1.79 nW and 1.50 nW for 735 nm and 850 nm, respectively. The ratio of the maximum NIR source power measurable without saturating the SiPD and NEP provided the dynamic optical range of 138 dB and 140 dB for 735 nm and 850 nm, respectively. This demonstrates that the system can measure a wide range of optical intensities. The average SNR of the above 50 dB was obtained for data from all NIR sources. The maximum SNR achieved was more than 64 dB. This shows that the designed system has good data acquisition ability, and all channels reached an SNR of over 40 dB. The average of the measured slope from all NIR sources showed an increase of less than 0.001% per sample, which is negligibly small. A full-frame sampling rate of 30 FPS was achieved. The sampling rate depends on the frame size (number of channels in the configuration) because the conventional spatial resolution may be used to find a region of interest before high-resolution imaging is utilized. A sampling rate of 2.4 kFPS was attained when the configuration was limited to 16 channels in the shape of a plus sign (+) with four channels on each side of SiPD. The use of a shielded cable ensures that the SiPD signal is not affected by other electronics in the system.

Low light intensities were adequate to acquire the SiPD signal from the forearm because the forearm is not encapsulated by the skull. The sphygmomanometer cuff was quickly filled with air on the upper arm to block the blood supply

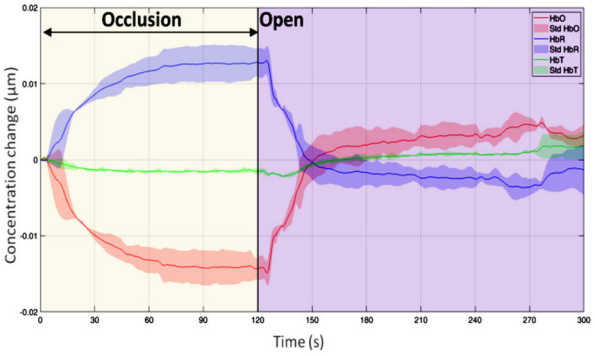

FIGURE 9. Average response of the arterial occlusion experiment at 240 mmHg.

to the forearm. A pressure of 240 mmHg was used to stop blood flow [26]. The time-series signal of HbO and HbR was computed using the raw intensity data acquired by the system under testing. Fig. 9 shows the mean and standard deviations of HbO, HbR, and HbT for all trials marked with occlusion and rest conditions. The graph shows the desired variations of HbO and HbR in-line with the expectations. The HbO signal can be seen to be decreasing during the duration of occlusion, while the HbR shows the same trend in the opposite direction. Once blood supply was resumed, HbO and HbR showed inverse behavior from the occlusion state, where the HbO increased and HbR decreased.

During data acquisition from the left motor cortex, higher gains were set by the device to achieve adequate signals from the NIR sources. All channels showed proper reception of light, and none of the channels was discarded during the configuration state. During the initial resting state, only signals of heartbeat and Mayer waves were expected from short-separation as well as long-separation channels. The resting-state data from the short-separation and long-separation channels showed similar variations in HbO because of the aforementioned signals. The similarity of short-separation and long-separation channels signifies the absence of any neuronal activity in the area under study. The HbO response for the motor task was observed because it is more reliable for activation detection [33]. The block-averaged HbO signals and standard deviations of 10 motor trials from a representative channel are shown in Fig. 10(b). During the task, the HbO signal was increased as anticipated, and it tended to reduce after the task was completed.

The hemodynamic response acquired from a short-separation channel can be used to remove the physiological signals from the long-separation channels. The results of short-separation-channel-based signal improvement are shown in Fig. 11, where the blue solid line represents the blocked averaged HbO value from a long-separated channel, the green dashed line indicates the signal from a short-separated channel, and the red dash-dotted line is the signal computed after applying the short-separation-based signal enhancement. The second peak shown in the blue curve during the task duration has been removed in the enhanced HbO signal.

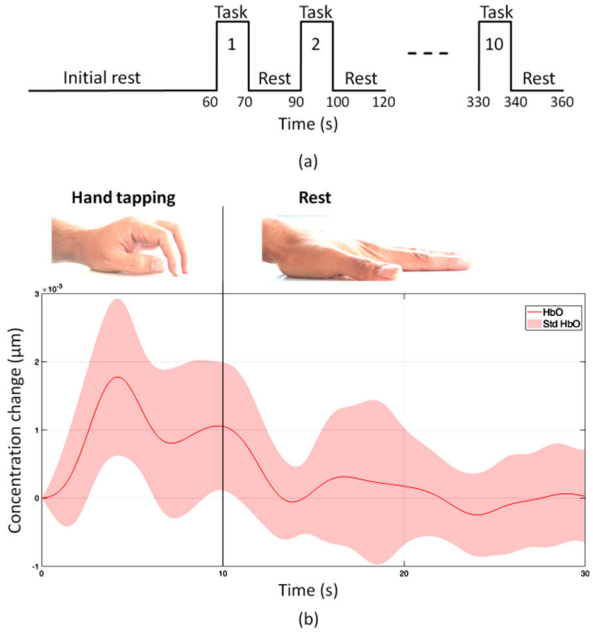

FIGURE 10. Hand tapping task: a) Paradigm, and b) block averaged HbO response of a representative channel.

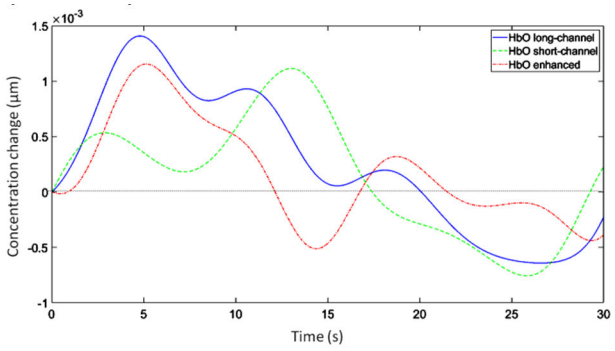

FIGURE 11. Short-separation-channel-based signal enhancement: The blue solid line is HbO from long-separated channel, the green dashed line is HbO from short-separated channel, and the red dash-dotted line shows the enhanced result of HbO from the blue line.

The system uses the automatic calibration of light intensities for every experiment such that the SiPD can receive stable light from all the channels. When a constant light intensity was used, the voltage produced by the photocurrent varied by the source-detector separation, as shown in Fig. 13(a). The LED-intensity adjustment circuit allows us to monitor the voltage produced in real-time until it reaches the required range. Fig. 13(b) shows the results obtained by adding real-time intensity control.

The developed software was also tested while being utilized to conduct the aforementioned testing procedures. The software was run on a computer with the specifications listed in Table 4. The software continuously showed HbO and HbR signals as well as the activation map without any interruptions for long durations while the subject kept working on the computer (duration up to 1 hr). The real-time display of an activation map and illustrative HbOs from 16 channels are shown in Fig. 12. The continuity of real-time display implies the stable working of the Wi-Fi module on the wearable device,

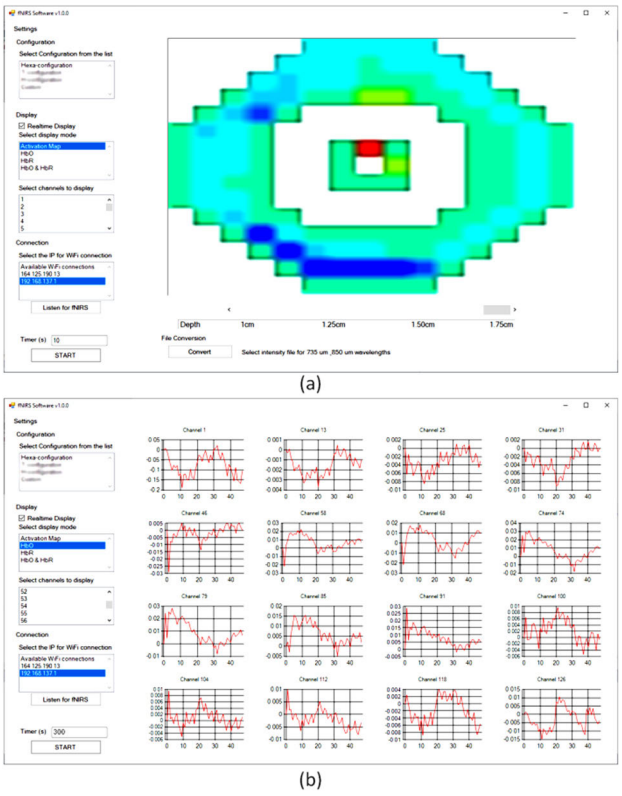

FIGURE 12. An example display when the subject worked on a computer: (a) An activation map and (b) HbO times-series for 16 channels.

providing continuous communication. The light intensity signals were converted to HbO and HbR by the conversion module of the software. The raw intensity data acquired for 960 s were converted to the desired chromophores and saved to a text file in less than 5.5 s.

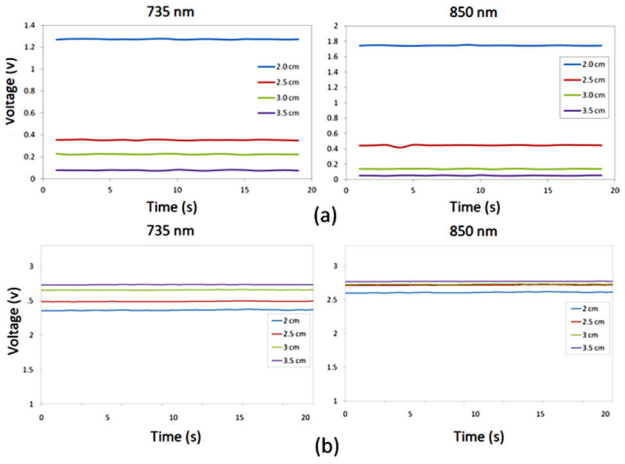

FIGURE 13. SiPD voltage: a) Without LED intensity gain circuit, and b) with LED intensity gain circuit.

IV. DISCUSSION

We described the development and technical evaluation of the developed fNIRS system. We focused on the design methodology to innovatively develop a wirelessly operated wearable device, which can perform real-time monitoring of

TABLE 4. Specifications of computer that hosts developed fNIRS software.

Operating system	Windows 10 pro 64-bit
Processor	Intel Core i5, 3.3 GHz
RAM	10 GB
Software environment	Microsoft Visual Studio Professional 2017

brain activation. The developed system caters to the need of comfort for the subject under study. The novel arrangement of sources and detector incorporates short-separation channels for providing robust brain imaging. The configuration allows the channels to reach multiple brain depths, which help construct a 3D brain activation map with high temporal resolution. The channels to be used in the study can be selected before the experiment. The system can add multiple devices to allow larger brain coverage. The system computes and displays the activation map and the desired chromophore levels in real-time. To the best of our knowledge, this is the first wearable device to incorporate this set of features. There exist some commercial systems providing hundreds of channels, however the size of their optodes and the detector saturation practically limit the number of channels in a local brain region. 3D printing was employed in fabricating the holders of LEDs and SiPD as well as the enclosure of the embedded system. The headgear is worn on the head while the embedded device can be worn like a backpack or tied to the upper arm. This allows the subject to comfortably perform the task in natural surroundings.

The system was tested under various experimental conditions for multiple characteristics. The results showed that the system could capture the light intensity over a wide range. The dynamic optical range measured was higher than that of previously reported devices (i.e., 80 dB in [52], 55 dB in [53], and 60 dB in [54], [55]). The device provided high SNR values for all the channels with different source-detector separations, and thus outperformed previously developed fNIRS devices (i.e., $>$ 40 dB in [52], and max 19 dB in [56]). An SNR of above 40 dB is required to provide robust hemodynamic response [57]. The minimum SNR of any channel reported by the developed device was more than 40 dB. The maximum source-detector separation in this device was above 38 mm, which is more than that of the conventional 30 mm. A stable signal with adequate value was acquired from all the channels when the experiment was conducted over the C3 region of the left motor cortex. The high SNR value can be attributed to the high power of LEDs being used [58]. The optical drift measured was below 0.001% per sample. The optical drift in this range does not affect the computation of our desired chromophores. This drift value is better than that of previously reported devices [26], [53]. The sampling rate of 30 FPS was considerably high, considering the slow nature of the hemodynamic response. A higher sampling rate is important in reducing noise factors.

Although the device has a higher number of optodes than conventional devices, the wearability of the system was the focus during design. The wearability can be attributed to the flexible 3D printed holder for LEDs and SiPD. The mobility of the real-time monitored system was ensured by the integration of a Wi-Fi connection. The compact design of the double-sided board for the prototype also ensured a small embedded device that could be easily worn and carried by the subject during the experiment. The embedded device encased in a 3D printed box can be placed in a backpack like previously developed systems or can be attached on the upper arm [24], [53], [58], [59]. The size of our 3D printed configuration holder was larger than some of the developed devices [26], [59], [60], but the number of optodes in the configuration was higher. If a comparison is drawn where an equal number of optodes is used, our configuration requires a substantially smaller area than other systems. Our configuration holder is smaller than the previously reported device montages [53], [55]. The size of the optode holder of a single source or detector (same size in our design) is smaller than most fNIRS systems [24], [58]. This allows the compact placement of a large number of optodes in a smaller area, resulting in an array-type of channels unlike that of any of the developed fNIRS devices. All or a few channels, based on the specifications of the investigation, can be selected, and multiple devices can be used to image large brain regions. Other developed fNIRS devices may reach 128 channels, but the spatial and temporal characteristics of the presented system are way beyond those of the other systems. The possibility of integrating EEG electrodes in the designed wearable device provides an additional advantage of multimodal imaging, a characteristic that has been recently employed for brain imaging [56], [61].

The hemodynamic response acquired during the motor execution task clearly showed neuronal activation phenomenon. A rise in HbO and a decline in HbR were observed, which agreed with the results of previously reported studies [24], [26]. The data from short-separated channels did not demonstrate similar hemodynamic response during the motor task. This showed that neuronal activation was captured from the deeper brain tissues and not from the extracerebral layers. An increase in HbO was observed in the short-separation channel, which is attributed to the blood perfusion occurring in response to the executed task [32], [62], [63]. The occurrence of a double peak in the HbO time-series while performing the task could be linked with the blood flow in the superficial layers [26]. Software for real-time chromophore computation and the display was not developed with previously reported devices [26], [53], [59], [60]. The utilization of a short-separation channel allows the filtering of physiological noises from the long-separated channels. Lately, various methodologies have been proposed to use the information from short-separation channels to improve fNIRS-based hemodynamic signals [34], [35]. Various software-based filtering schemes have been conventionally used [34], [36]. These methods are complex and usually require high computation power (which is not a major concern nowadays because of the widely available high-tech computers); nevertheless, they cannot exactly match the physiological

information directly. Multiple biomedical devices can be used to measure pulse, respiration, blood pressure, and skin conductance while performing an fNIRS-based study [64]. However, this requires an additional experimental setup, which was seamlessly performed by the integration of short-separation channels. Short separation channels also reduce any additional hardware for reducing motion artifacts as it also captures their effect along with physiological signals [65]. In addition, the mobility and wearability achieved by the presented device can be hampered depending on the characteristics of these biomedical devices.

The creation of a 3D image of the brain is critical for clinical diagnosis. fNIRS has already shown the results in disease diagnosis [66]. However, specifying a local region in the brain responsible for the disease is yet to be done. Various tomographic techniques have been used in the literature for the generation of a 3D image based on the hemodynamic signals [8], [67], [68]. The activation maps of two fingers were distinguished during the somatotopic stimulation task using an ultra-high density tomography approach [67]. The results of activation mapping were compared with fMRI to find closely matching results in the 3D space, which showed the possibility of utilizing fNIRS systems for creating a robust 3D image. Furthermore, the topographic approaches differ based on regularization techniques and their criteria. A comprehensive analysis of the result of various tomography approaches was conducted, including linearly constrained minimum variance, minimum $\{l_0, l_1,$ and $l_2\}$-norm estimate, depth- and noise-weighted minimum norm, spatial flexibility, and truncated singular value decomposition [68]. The analysis of these methods concluded that linear methods provide fast and adequate results. In the developed system, the bundled-optode technique is used that takes assumption about depth being equal to half of the source-detector separation [38], [47]. Laterally, the center of the vector from a source to a detector represents the location. By combining the depth and lateral information, we can generate a 3D image of the brain's neuronal activation. The bundled-optode technique has shown to effectively identify the neuronal activation in a local brain region with less computational power than other tomographic approaches.

The device can be further advanced by adding more SiPDs. The addition of a single SiPD will double the current number of channels. The device can be used on subjects without hair. The use of optical fibers as a light guide between the scalp and the optodes will allow the seamless application of the system on hairy surfaces. Further miniaturization of the system is possible by stacking multiple electronic boards inside a smaller box, which can be attached directly with the headgear. This will reduce the length of wires between the embedded device and headgear, thus improving the robustness of the system. EEG electrodes will be integrated to exhibit multimodality. The optode configuration can be modified such that the channel locations can become uniform in the x-, y-, and z-directions. This will enhance 3D image reconstruction. A uniform 3D imaging for the full head should be the target, which can be comparable with fMRI up to the physical depth limit of fNIRS. Therefore, a single unit for whole-brain imaging is anticipated in the future.

V. CONCLUSION

We designed and developed a novel fNIRS system that provides a working combination of prominent characteristics. The system is wearable, includes channels that reach different depths in the brain to provide a 3D image, allows channel selection, has a significantly higher spatial density along with sufficient temporal resolution, and provides a real-time display of acquired chromophores (HbO and HbR). Multiple modules can be used to cover a large brain area, while a single module covers an area of 7×7 cm. The Wi-Fi-based system allows the subject to move freely during the experiment, which favors its utilization for BCI. The integration of short-separation channels allows efficient removal of physiological noise present in the fNIRS signal. The system characteristics measured through the phantom tests showed higher values when compared with the existing devices in the literature. The chromophores were also acquired during multiple paradigms on a human subject, which provided the anticipated results. The system offers high-definition imaging with a large number of channels (128 channels) to cover a local brain region, which will help clinicians and researchers monitor and measure brain activity indoors and outdoors. There is no wearable fNIRS system that incorporates these characteristics, especially the bundled type arrangement of 129 sources and detector. The developed system will allow the healthcare industry to perform continuous brain-state monitoring of the rising number of patients with various brain diseases in an economically feasible manner.

ACKNOWLEDGMENT

MAY developed the system, and wrote the first draft of the manuscript. S-WW assisted MAY in device development. K-SH has suggested the design aspects of the study, corrected the manuscript, and supervised all the process from the beginning. All authors have approved the final manuscript.

REFERENCES

[1] M. J. Prince, "World Alzheimer report 2015: The global impact of dementia: An analysis of prevalence, incidence, cost and trends," Alzheimer's Disease Int., London, U.K., Tech. Rep., 2015, p. 8.
[2] N. K. Logothetis, "What we can do and what we cannot do with fMRI," *Nature*, vol. 453, no. 7197, pp. 869–878, Jun. 2008.
[3] A.-C. Ehlis, S. Schneider, T. Dresler, and A. J. Fallgatter, "Application of functional near-infrared spectroscopy in psychiatry," *NeuroImage*, vol. 85, pp. 478–488, Jan. 2014.
[4] G. Strangman, J. P. Culver, J. H. Thompson, and D. A. Boas, "A quantitative comparison of simultaneous BOLD fMRI and NIRS recordings during functional brain activation," *NeuroImage*, vol. 17, no. 2, pp. 719–731, Oct. 2002.
[5] A. Zafar and K.-S. Hong, "Neuronal activation detection using vector phase analysis with dual threshold circles: A functional near-infrared spectroscopy study," *Int. J. Neural Syst.*, vol. 28, no. 10, Dec. 2018, Art. no. 1850031.
[6] M. Ferrari and V. Quaresima, "A brief review on the history of human functional near-infrared spectroscopy (fNIRS) development and fields of application," *NeuroImage*, vol. 63, no. 2, pp. 921–935, Nov. 2012.

[7] M. J. Khan, U. Ghafoor, and K.-S. Hong, "Early detection of hemodynamic responses using EEG: A hybrid EEG-fNIRS study," *Frontiers Hum. Neurosci.*, vol. 12, Nov. 2018, Art. no. 479.

[8] H. Dehghani, B. R. White, B. W. Zeff, A. Tizzard, and J. P. Culver, "Depth sensitivity and image reconstruction analysis of dense imaging arrays for mapping brain function with diffuse optical tomography," *Appl. Opt.*, vol. 48, no. 10, pp. D137–D143, 2009.

[9] G. E. Strangman, Z. Li, and Q. Zhang, "Depth sensitivity and source-detector separations for near infrared spectroscopy based on the Colin27 brain template," *PLoS ONE*, vol. 8, no. 8, Aug. 2013, Art. no. e66319.

[10] G. Wang, Z. Liu, Y. Feng, J. Li, H. Dong, D. Wang, J. Li, N. Yan, T. Liu, and X. Yan, "Monitoring the depth of anesthesia through the use of cerebral hemodynamic measurements based on sample entropy algorithm," *IEEE Trans. Biomed. Eng.*, vol. 67, no. 3, pp. 807–816, Mar. 2020.

[11] Y. Zheng, D. Zhang, L. Wang, Y. Wang, H. Deng, S. Zhang, D. Li, and D. Wang, "Resting-state-based spatial filtering for an fNIRS-based motor imagery brain-computer interface," *IEEE Access*, vol. 7, pp. 120603–120615, 2019.

[12] D. T. Delpy, M. Cope, P. V. D. Zee, S. Arridge, S. Wray, and J. Wyatt, "Estimation of optical pathlength through tissue from direct time of flight measurement," *Phys. Med. Biol.*, vol. 33, no. 12, pp. 1433–1442, Dec. 1988.

[13] L. Kocsis, P. Herman, and A. Eke, "The modified Beer–Lambert law revisited," *Phys. Med. Biol.*, vol. 51, no. 5, pp. N91–N98, 2006.

[14] M. A. Yaqub, S.-W. Woo, and K.-S. Hong, "Effects of HD-tDCS on resting-state functional connectivity in the prefrontal cortex: An fNIRS study," *Complexity*, vol. 2018, Nov. 2018, Art. no. 1613402.

[15] Y. Zhu, J. K. Jayagopal, R. K. Mehta, M. Erraguntla, J. Nuamah, A. D. McDonald, H. Taylor, and S.-H. Chang, "Classifying major depressive disorder using fNIRS during motor rehabilitation," *IEEE Trans. Neural Syst. Rehabil. Eng.*, vol. 28, no. 4, pp. 961–969, Apr. 2020.

[16] S. Coyle, T. Ward, C. Markham, and G. McDarby, "On the suitability of near-infrared (NIR) systems for next-generation brain–computer interfaces," *Physiological Meas.*, vol. 25, no. 4, pp. 815–822, Aug. 2004.

[17] X. Jiang, X. Gu, K. Xu, H. Ren, and W. Chen, "Independent decision path fusion for bimodal asynchronous brain–computer interface to discriminate multiclass mental states," *IEEE Access*, vol. 7, pp. 165303–165317, 2019.

[18] R. Hosseini, B. Walsh, F. Tian, and S. Wang, "An fNIRS-based feature learning and classification framework to distinguish hemodynamic patterns in children who stutter," *IEEE Trans. Neural Syst. Rehabil. Eng.*, vol. 26, no. 6, pp. 1254–1263, Jun. 2018.

[19] K.-S. Hong and A. Zafar, "Existence of initial dip for BCI: An illusion or reality," *Frontiers Neurorobotics*, vol. 12, Oct. 2018, Art. no. 69.

[20] A.-K. Seghouane and D. Ferrari, "Robust hemodynamic response function estimation from fNIRS signals," *IEEE Trans. Signal Process.*, vol. 67, no. 7, pp. 1838–1848, Apr. 2019.

[21] H. Tanaka, T. Katura, and H. Sato, "Task-related component analysis for functional neuroimaging and application to near-infrared spectroscopy data," *NeuroImage*, vol. 64, pp. 308–327, Jan. 2013.

[22] F. Scholkmann, S. Kleiser, A. J. Metz, R. Zimmermann, J. M. Pavia, U. Wolf, and M. Wolf, "A review on continuous wave functional near-infrared spectroscopy and imaging instrumentation and methodology," *NeuroImage*, vol. 85, pp. 6–27, Jan. 2014.

[23] Y. Xu, L. Zhang, and C. Wang, "A rapid detection system design for escherichia coli in food based on a nanoprobe and graphite electrode coupled with ATP bioluminescence technology," *IEEE Access*, vol. 7, pp. 106882–106889, 2019.

[24] M. J. Saikia, W. G. Besio, and K. Mankodiya, "WearLight: Toward a wearable, configurable functional NIR spectroscopy system for noninvasive neuroimaging," *IEEE Trans. Biomed. Circuits Syst.*, vol. 13, no. 1, pp. 91–102, Feb. 2019.

[25] H. Zhao and R. J. Cooper, "Review of recent progress toward a fiberless, whole-scalp diffuse optical tomography system," *Neurophotonics*, vol. 5, no. 1, Sep. 2017, Art. no. 011012.

[26] D. Wyser, O. Lambercy, F. Scholkmann, M. Wolf, and R. Gassert, "Wearable and modular functional near-infrared spectroscopy instrument with multidistance measurements at four wavelengths," *Neurophotonics*, vol. 4, no. 4, Aug. 2017, Art. no. 041413.

[27] J. Shin, J. Kwon, J. Choi, and C.-H. Im, "Ternary near-infrared spectroscopy brain-computer interface with increased information transfer rate using prefrontal hemodynamic changes during mental arithmetic, breath-holding, and idle state," *IEEE Access*, vol. 6, pp. 19491–19498, 2018.

[28] N. H. Kashou and B. M. Giacherio, "Stimulus and optode placement effects on functional near-infrared spectroscopy of visual cortex," *Neurophotonics*, vol. 3, no. 2, Jun. 2016, Art. no. 025005.

[29] K.-S. Hong and M. A. Yaqub, "Application of functional near-infrared spectroscopy in the healthcare industry: A review," *J. Innov. Opt. Health Sci.*, vol. 12, no. 06, Nov. 2019, Art. no. 1930012.

[30] R. J. Cooper, J. Selb, L. Gagnon, D. Phillip, H. W. Schytz, H. K. Iversen, M. Ashina, and D. A. Boas, "A systematic comparison of motion artifact correction techniques for functional near-infrared spectroscopy," *Frontiers Neurosci.*, vol. 6, Oct. 2012, Art. no. 147.

[31] X. Cui, S. Bray, and A. L. Reiss, "Functional near infrared spectroscopy (NIRS) signal improvement based on negative correlation between oxygenated and deoxygenated hemoglobin dynamics," *NeuroImage*, vol. 49, no. 4, pp. 3039–3046, Feb. 2010.

[32] I. Tachtsidis and F. Scholkmann, "False positives and false negatives in functional near-infrared spectroscopy: Issues, challenges, and the way forward," *Neurophotonics*, vol. 3, no. 3, Mar. 2016, Art. no. 031405.

[33] U. Ghafoor, J.-H. Lee, K.-S. Hong, S.-S. Park, J. Kim, and H.-R. Yoo, "Effects of acupuncture therapy on MCI patients using functional near-infrared spectroscopy," *Frontiers Aging Neurosci.*, vol. 11, Aug. 2019, Art. no. 237.

[34] P. Pinti, F. Scholkmann, A. Hamilton, P. Burgess, and I. Tachtsidis, "Current status and issues regarding pre-processing of fNIRS neuroimaging data: An investigation of diverse signal filtering methods within a general linear model framework," *Frontiers Human Neurosci.*, vol. 12, Jan. 2019, Art. no. 505.

[35] S. Brigadoi and R. J. Cooper, "How short is short? Optimum source–detector distance for short-separation channels in functional near-infrared spectroscopy," *Neurophotonics*, vol. 2, no. 2, May 2015, Art. no. 025005.

[36] Q. Zhang, E. N. Brown, and G. E. Strangman, "Adaptive filtering for global interference cancellation and real-time recovery of evoked brain activity: A Monte Carlo simulation study," *J. Biomed. Opt.*, vol. 12, no. 4, 2007, Art. no. 044014.

[37] R. B. Saager and A. J. Berger, "Direct characterization and removal of interfering absorption trends in two-layer turbid media," *J. Opt. Soc. Amer. A, Opt. Image Sci.*, vol. 22, no. 9, pp. 1874–1882, 2005.

[38] H. D. Nguyen and K.-S. Hong, "Bundled-optode implementation for 3D imaging in functional near-infrared spectroscopy," *Biomed. Opt. Express*, vol. 7, no. 9, pp. 3491–3507, 2016.

[39] A. T. Eggebrecht, S. L. Ferradal, A. Robichaux-Viehoever, M. S. Hassanpour, H. Dehghani, A. Z. Snyder, T. Hershey, and J. P. Culver, "Mapping distributed brain function and networks with diffuse optical tomography," *Nature Photon.*, vol. 8, no. 6, pp. 448–454, Jun. 2014.

[40] X. Li, J.-A. Fang, and H. Li, "Exponential synchronization of stochastic memristive recurrent neural networks under alternate state feedback control," *Int. J. Control, Autom. Syst.*, vol. 16, no. 6, pp. 2859–2869, Dec. 2018.

[41] J. Moon, H. Kim, and B. Lee, "View-point invariant 3D classification for mobile robots using a convolutional neural network," *Int. J. Control, Autom. Syst.*, vol. 16, no. 6, pp. 2888–2895, Dec. 2018.

[42] T. Trakoolwilaiwan, B. Behboodi, J. Lee, K. Kim, and J.-W. Choi, "Convolutional neural network for high-accuracy functional near-infrared spectroscopy in a brain–computer interface: Three-class classification of rest, right-, and left-hand motor execution," *Neurophotonics*, vol. 5, no. 1, Sep. 2017, Art. no. 011008.

[43] Q. C. Nguyen, M. Piao, and K.-S. Hong, "Multivariable adaptive control of the rewinding process of a Roll-to-roll system governed by hyperbolic partial differential equations," *Int. J. Control, Autom. Syst.*, vol. 16, no. 5, pp. 2177–2186, Oct. 2018.

[44] D. Arifler, T. Zhu, S. Madaan, and I. Tachtsidis, "Optimal wavelength combinations for near-infrared spectroscopic monitoring of changes in brain tissue hemoglobin and cytochrome c oxidase concentrations," *Biomed. Opt. Express*, vol. 6, no. 3, pp. 933–947, 2015.

[45] K. Uludağ, J. Steinbrink, A. Villringer, and H. Obrig, "Separability and cross talk: Optimizing dual wavelength combinations for near-infrared spectroscopy of the adult head," *NeuroImage*, vol. 22, no. 2, pp. 583–589, Jun. 2004.

[46] G. Strangman, M. A. Franceschini, and D. A. Boas, "Factors affecting the accuracy of near-infrared spectroscopy concentration calculations for focal changes in oxygenation parameters," *NeuroImage*, vol. 18, no. 4, pp. 865–879, Apr. 2003.

[47] H.-D. Nguyen, K.-S. Hong, and Y.-I. Shin, "Bundled-optode method in functional near-infrared spectroscopy," *PLoS ONE*, vol. 11, no. 10, Oct. 2016, Art. no. e0165146.

[48] F. Herold, P. Wiegel, F. Scholkmann, and N. Müller, "Applications of functional near-infrared spectroscopy (fNIRS) neuroimaging in exercise–cognition science: A systematic, methodology-focused review," *J. Clin. Med.*, vol. 7, no. 12, p. 466, Nov. 2018.

[49] S. Brigadoi, L. Ceccherini, S. Cutini, F. Scarpa, P. Scatturin, J. Selb, L. Gagnon, D. A. Boas, and R. J. Cooper, "Motion artifacts in functional near-infrared spectroscopy: A comparison of motion correction techniques applied to real cognitive data," *NeuroImage*, vol. 85, pp. 181–191, Jan. 2014.

[50] K.-S. Hong, M. R. Bhutta, X. Liu, and Y.-I. Shin, "Classification of somatosensory cortex activities using fNIRS," *Behavioural Brain Res.*, vol. 333, pp. 225–234, Aug. 2017.

[51] L. Huang, W. C. Tan, L. Wang, B. Dong, C. Lee, and K.-W. Ang, "Infrared black phosphorus phototransistor with tunable responsivity and low noise equivalent power," *ACS Appl. Mater. Interfaces*, vol. 9, no. 41, pp. 36130–36136, Oct. 2017.

[52] D. Chitnis, D. Airantzis, D. Highton, R. Williams, P. Phan, V. Giagka, S. Powell, R. J. Cooper, I. Tachtsidis, M. Smith, C. E. Elwell, J. C. Hebden, and N. Everdell, "Towards a wearable near infrared spectroscopic probe for monitoring concentrations of multiple chromophores in biological tissue *in vivo*," *Rev. Sci. Instrum.*, vol. 87, no. 6, Jun. 2016, Art. no. 065112.

[53] A. von Lühmann, C. Herff, D. Heger, and T. Schultz, "Toward a wireless open source instrument: Functional near-infrared spectroscopy in mobile neuroergonomics and BCI applications," *Frontiers Hum. Neurosci.*, vol. 9, Nov. 2015, Art. no. 617.

[54] U. Ha, J. Lee, M. Kim, T. Roh, S. Choi, and H.-J. Yoo, "An EEG-NIRS multimodal SoC for accurate anesthesia depth monitoring," *IEEE J. Solid-State Circuits*, vol. 53, no. 6, pp. 1830–1843, Jun. 2018.

[55] J.-K. Choi, J.-M. Kim, G. Hwang, J. Yang, M.-G. Choi, and H.-M. Bae, "Time-divided spread-spectrum code-based 400 fW-detectable multichannel fNIRS IC for portable functional brain imaging," *IEEE J. Solid-State Circuits*, vol. 51, no. 2, pp. 484–495, Feb. 2016.

[56] E. Lareau, F. Lesage, P. Pouliot, D. Nguyen, J. L. Lan, and M. Sawan, "Multichannel wearable system dedicated for simultaneous electroencephalography/near-infrared spectroscopy real-time data acquisitions," *J. Biomed. Opt.*, vol. 16, no. 9, 2011, Art. no. 096014.

[57] R. Pagano, S. Libertino, D. Sanfilippo, G. Fallica, and S. Lombardo, "Improvement of sensitivity in continuous wave near infra-red spectroscopy systems by using silicon photomultipliers," *Biomed. Opt. Express*, vol. 7, no. 4, pp. 1183–1192, 2016.

[58] S. K. Piper, A. Krueger, S. P. Koch, J. Mehnert, C. Habermehl, J. Steinbrink, H. Obrig, and C. H. Schmitz, "A wearable multi-channel fNIRS system for brain imaging in freely moving subjects," *NeuroImage*, vol. 85, pp. 64–71, Jan. 2014.

[59] R. McKendrick, R. Parasuraman, and H. Ayaz, "Wearable functional near infrared spectroscopy (fNIRS) and transcranial direct current stimulation (tDCS): Expanding vistas for neurocognitive augmentation," *Frontiers Syst. Neurosci.*, vol. 9, Mar. 2015, Art. no. 27.

[60] D. Chitnis, R. J. Cooper, L. Dempsey, S. Powell, S. Quaggia, D. Highton, C. Elwell, J. C. Hebden, and N. L. Everdell, "Functional imaging of the human brain using a modular, fibre-less, high-density diffuse optical tomography system," *Biomed. Opt. Express*, vol. 7, no. 10, p. 4275, 2016.

[61] J. W. Li, S. Barma, P. U. Mak, S. H. Pun, and M. I. Vai, "Brain rhythm sequencing using EEG signals: A case study on seizure detection," *IEEE Access*, vol. 7, pp. 160112–160124, 2019.

[62] S. Keshmiri, H. Sumioka, M. Okubo, and H. Ishiguro, "An information-theoretic approach to quantitative analysis of the correspondence between skin blood flow and functional near-infrared spectroscopy measurement in prefrontal cortex activity," *Frontiers Neurosci.*, vol. 13, Feb. 2019, Art. no. 79.

[63] S. Kohno, I. Miyai, A. Seiyama, I. Oda, A. Ishikawa, S. Tsuneishi, T. Amita, and K. Shimizu, "Removal of the skin blood flow artifact in functional near-infrared spectroscopic imaging data through independent component analysis," *J. Biomed. Opt.*, vol. 12, no. 6, 2007, Art. no. 062111.

[64] R. Zimmermann, L. Marchal-Crespo, J. Edelmann, O. Lambercy, M.-C. Fluet, R. Riener, M. Wolf, and R. Gassert, "Detection of motor execution using a hybrid fNIRS-biosignal BCI: A feasibility study," *J. Neuro-Eng. Rehabil.*, vol. 10, Jan. 2013, Art. no. 4.

[65] Q. Zhang, X. Yan, and G. E. Strangman, "Development of motion resistant instrumentation for ambulatory near-infrared spectroscopy," *J. Biomed. Opt.*, vol. 16, no. 8, 2011, Art. no. 087008.

[66] L. Gao, Y. Cai, H. Wang, G. Wang, Q. Zhang, and X. Yan, "Probing prefrontal cortex hemodynamic alterations during facial emotion recognition for major depression disorder through functional near-infrared spectroscopy," *J. Neural Eng.*, vol. 16, no. 2, Apr. 2019, Art. no. 026026.

[67] C. Habermehl, S. Holtze, J. Steinbrink, S. P. Koch, H. Obrig, J. Mehnert, and C. H. Schmitz, "Somatosensory activation of two fingers can be discriminated with ultrahigh-density diffuse optical tomography," *NeuroImage*, vol. 59, no. 4, pp. 3201–3211, Feb. 2012.

[68] C. Habermehl, J. Steinbrink, K.-R. Müller, and S. Haufe, "Optimizing the regularization for image reconstruction of cerebral diffuse optical tomography," *J. Biomed. Opt.*, vol. 19, no. 9, Sep. 2014, Art. no. 096006.

M. ATIF YAQUB received the B.S. degree in electrical engineering from the Center for Advanced Studies in Engineering, Islamabad, Pakistan, in 2008, and the M.S. degree in electrical engineering from Universiti Tun Hussein Onn Malaysia, Malaysia, in 2012. He is currently pursuing the Ph.D. degree with the School of Mechanical Engineering, Pusan National University, Busan, South Korea. His research interests include embedded system design, fNIRS-based brain imaging, neuromodulation, and brain-computer interfaces.

SEONG-WOO WOO received the B.S. and M.S. degrees from the School of Mechanical Engineering, Pusan National University, Busan, South Korea, in 2016 and 2019, respectively, where he is currently pursuing the Ph.D. degree. His research interests include machine learning, multimodal neuroimaging, and brain-computer interfaces.

KEUM-SHIK HONG (Fellow, IEEE) received the B.S. degree in mechanical design and production engineering from Seoul National University, in 1979, the M.S. degree in mechanical engineering from Columbia University, New York, NY, USA, in 1987, and the M.S. degree in applied mathematics and the Ph.D. degree in mechanical engineering from the University of Illinois at Urbana-Champaign (UIUC), in 1991. He joined the School of Mechanical Engineering, Pusan National University (PNU), in 1993. His Integrated Dynamics and Control Engineering Laboratory was designated a National Research Laboratory by the Ministry of Science and Technology of Korea, in 2003. In 2009, under the auspices of the World Class University Program of the Ministry of Education, Science and Technology (MEST) of Korea, he established the Department of Cogno-Mechatronics Engineering, PNU. His current research interests include brain-computer interface, nonlinear systems theory, adaptive control, distributed parameter systems, autonomous vehicles, and innovative control applications in brain engineering. He was the past President of the Institute of Control, Robotics and Systems (ICROS), South Korea, and is the President-Elect of the Asian Control Association. He was the Organizing Chair of the ICROS-SICE International Joint Conference 2009, Fukuoka, Japan. He is a Fellow of the Korean Academy of Science and Technology, an ICROS Fellow, a member of the National Academy of Engineering of Korea, and many other societies. He has received many awards, including the Best Paper Award from the KFSTS of Korea (1999), the F. Harashima Mechatronics Award (2003), the IJCAS Scientific Activity Award (2004), the Automatica Certificate of Outstanding Service (2006), the Presidential Award of Korea (2007), the ICROS Achievement Award (2009), the IJCAS Contribution Award (2010), the Premier Professor Award (2011), the JMST Contribution Award (2011), the IJCAS Contribution Award (2011), the IEEE Academic Award of ICROS (2016), and so on. He has served as an Associate Editor for *Automatica* (2000–2006), the Editor-in-Chief of the *Journal of Mechanical Science and Technology* (2008–2011), and is currently serving as the Editor-in-Chief of the *International Journal of Control, Automation, and Systems*.